# Effects of air bubbles on underwater optical wireless communication [Invited]

**Daomin Chen (陈道敏), Jiemei Wang (王介梅), Shangbin Li (李上宾), and Zhengyuan Xu (徐正元)***

*CAS Key Laboratory of Wireless-Optical Communications, University of Science and Technology of China, Hefei 230027, China*

**Corresponding author: xuzy@ustc.edu.cn*

Received July 13, 2019; accepted September 10, 2019; posted online October 8, 2019

The received signal intensity fluctuation and communication performance of an underwater optical wireless communication (UOWC) system under the air bubble effects are experimentally investigated. For different bubble density and size, lognormal, gamma, Weibull, and generalized extreme value distributions are tested to fit the fluctuation of the signal intensity at the receiving end. The best fitting distribution is found to vary with bubble parameters. The communication system performance with on–off keying and pulse position modulation is further studied.

*OCIS codes: 060.4510, 010.0010, 270.2500.*
*doi: 10.3788/COL201917.100008.*

Most of the earth is covered by water, while human activities take place only on 29% of its surface. The exploration of the ocean has become ever important for deep understanding of creature evolution, natural resource development, and national security. Information and communication technologies play critical roles in assisting such activities reaching the marine field. Applications include information exchange among autonomous underwater vehicles (AUVs), submarines, and ships on the water surface. In addition to machine communication, human communication is also an important aspect, among divers or between a diver and people on board, in location tracking of underwater athletes, and so on.

In an underwater environment, long-wave radio frequency and underwater acoustic communications are two major wireless communication technologies. Different from traditional underwater wireless communication, the rising underwater optical wireless communication (UOWC) offers advantages in broad bandwidth, high data rate, low latency, anti-interference, and high security[1–4]. It, thus, attracts more and more attention recently. Due to the complexity of an underwater environment, design and construction of a reliable and highly stable UOWC system requires comprehensive knowledge of transmission characteristics of an underwater channel and associated communication techniques.

Compared with channel characterization and system design, there are limited studies on the impacts of air bubbles on the channel and communication system performance. In 1988, Dean's team investigated the light dispersion effects near the critical point and Brewster scattering angles in the presence of bubbles[5]. In 1998, Holt's team studied the light intensity and bubble response (bubbles near the light threshold caused by single-bubble sounds) at the water–air interface[6]. In 2006, Wang's team adopted a traditional Monte-Carlo method and established a model toward a micron-order bubble group with relatively longer survival time in the wake flow of the ship[7]. In 2007, Yuan's team provided the size distribution of the bubble on the ocean surface caused by waves[8]. Fickenscher's team revealed the performance of an underwater optical wireless sensor network in the presence of bubbles in 2012[9]. Recently in 2017, Oubei and co-authors studied the effects of bubble size and density on the UOWC quality. They found that the bubble size and density caused deep fading of the signal and proposed beam broadening techniques to improve the communication performance[10]. Salehi and his team members presented comprehensive experimental fitting results of statistical fading distributions in the presence of air bubbles using an aperture averaging lens (AAL) and ultraviolet visible photodetector at the receiver to capture the optical irradiance[11]. They successfully associated seven types of distribution models to a large range of the scintillation index and found the predictable fitting models. Although the scintillation index is a well-known controlling parameter to describe turbulence severity in the atmosphere, their results offered significantly valuable insight into the statistical behavior of underwater turbulence for a variety of scenarios for the first time, to the best of our knowledge. They also proposed an effective multiple input multiple output (MIMO) configuration to effectively mitigate turbulence for a UOWC channel[12].

This Letter focuses on the effects of bubbles on the UOWC channel and system performance in terms of bubble density, bubble size, and data modulation. Motivated by but different from the work for bubbly channel turbulence[11], we adopt a commercial camera as the optical-to-electrical convertor, which can easily capture intensity fluctuations and facilitate subsequent data analysis. Meanwhile, we directly associate bubble density and bubble size to signal distributions, building a close link

 

between the physical conditions and intensity statistics. From measurements of the received signal intensity, we found the corresponding models to describe and fit the intensity fluctuation.

The experimental platform with controllable bubbles for UOWC is shown in Fig. 1. At the transmitter, an arbitrary waveform generator (AWG) generates the electrical signals that are combined with a direct current (DC) via a bias-tee and injected into the laser diode (LD) source (Thorlabs, LP520-SF15). In such a way, the electrical signals are converted to optical signals for underwater transmission. After collimation and beam expansion (Thorlabs, BE05-10-A), the optical signals are transmitted into the underwater bubble channel. The size of the water tank is 1 m × 1 m × 0.7 m. The bottom of the experimental platform is equipped with 5 mm, 8 mm, 10 mm, and 12 mm copper pipes, connected to an air pump. Bubbles of different density and size can be generated by changing the power of the air pump and the diameter of the copper pipe. Light transmitted through the underwater channel is focused by a condenser lens at the receiver on the opposite side of the transmitter. A high speed visible light camera module converts the received optical signals into grayscale images for offline processing so that the fluctuation of the received signals can be analyzed. To study the communication system quality, an avalanche photodetector (APD) module (Thorlabs, APD210) is used to convert the received optical signals into electrical signals and is then sent to the oscilloscope (OSC) for data acquisition and further signal processing. The APD module has high sensitivity and 3 dB bandwidth of 1 GHz.

In the experiment, the relative density and size of generated bubbles were controlled by the predetermined air pipe size and air pump power. When changing the bubble density, we fixed the predetermined air pipe size (0.3 mm) and changed the air pump power. Similarly, when changing the bubble size, we fixed the air pump power and changed the size of the generated bubbles by changing the predetermined air pipe size. Using a high speed visible light camera to take grayscale images, we found their correspondences with the grade of the air flow rate.

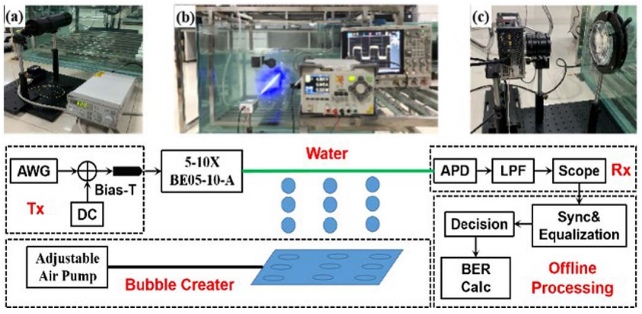


Fig. 1. Experimental platform with controllable bubbles for UOWC: (a) transmitter, (b) water channel with controllable bubble generation, (c) receiver of high speed visible light camera/APD.

We partitioned the air flow rate uniformly into 16 grades from 0× to 15× at a step size of 3×, where 15× corresponds to the maximum power of the air pump of 16 W, and 0× corresponds to the minimum power. Relevant results are shown in Table 1. For the density results, the bubble size is fixed to about 0.3 mm, and light beam size is about 2.8 mm. The density is a measure to count the number of bubbles in unit time. The bubble size also takes 16 different values.

As can be seen from Table 1, the bubble density varies almost linearly with the grade of the air flow rate, as the power increases from the beginning, but it tends to saturate as the pump approaches its maximum capacity. Similar trends can be observed for the bubble size. The actual bubble density and size depend on the power of the air pump and the aperture size of the air pipe. When the output aperture size of the bubble remains unchanged and the power of the air pump varies at equal intervals of 0–16 W, about 0–40 bubbles within an observation time window can be generated to pass through the optical transmission path. By changing the aperture size of the copper air pipe and adjusting the power of the air pump, bubbles of different densities and sizes can be generated. The maximum diameter of the observable bubbles is 2.8 mm. The bubbles larger than the light beam size are not observable as indicated in the table.

We measured the received signal intensities under different bubble density and bubble size. For each parameter setting, 5000 gray images of each bubble along the bubble flow path were taken. Figures 2 and 3 depict graphically typical gray images when bubble density and bubble size

**Table 1.** Bubble Density and Size in Different Grades of Air Flow Rate

| N× | 0× | 3× | 6× | 9× | 12× | 15× |
|---|---|---|---|---|---|---|
| Bubble Density $P_{\text{Bubble}}$ | 0 | 9–12 | 23–27 | 27–33 | 32–38 | 35–38 |
| N× | 0× | 3× | 6× | 9× | 12× | 15× |
| Bubble Size (mm) $D_{\text{Bubble}}$ | 0 | 1.2 | 1.8 | 2.5 | >2.8 | >2.8 |

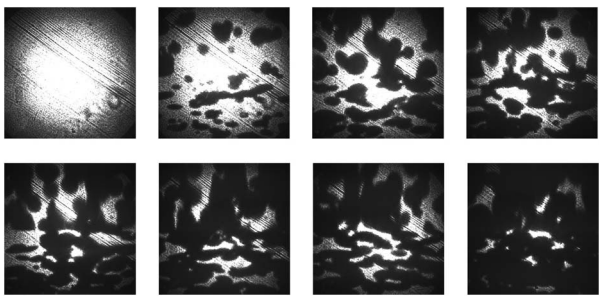

Fig. 2. Series of gray images as bubble density increases.

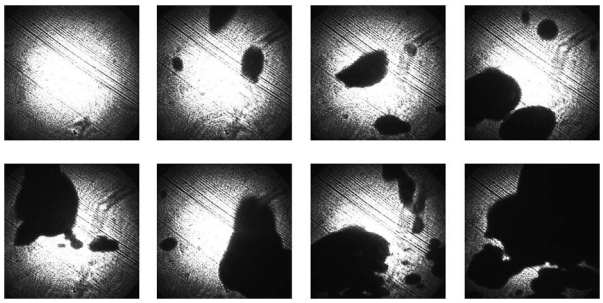

Fig. 3. Series of gray images as bubble size increases.

increase from the minimum to the allowable maximum, respectively. The gray values were recorded and normalized by the total power of each image. Then, measured distribution (MD) was obtained from measured samples. We have fitted the existing statistical distribution models with received signal intensity fluctuation in the scenarios of different bubble density and size. We similarly define the scintillation index as follows[11]:

$$\sigma_I^2=\frac{E[I^2]-E^2[I]}{E^2[I]}, \tag{1}$$

where $I$ is the instantaneous light intensity at the receiver, and $E$ denotes the expected value. Our experimental results show that the intensity scintillation index at the receiver is less than 0.03 when the bubble density changes. Therefore, we adopted some well-known signal distributions under atmospheric turbulence in free space optical communication to model received signal intensity fluctuation when the bubble density changes, including lognormal distribution (LD), gamma distribution (GD), Weibull distribution (WD), and generalized extreme value distribution (GEVD).

In order to test the fitting accuracy of different distribution models with experimental data in different bubble density and size, we adopt the following goodness of fit (GoF) metric, also known as the $R^2$ measure[11,13,14]:

$$R^2=1-\frac{\sum_{i=1}^{M}(f_{m.i}-f_{p,i})^2}{\sum_{i=1}^{M}(f_{m.i}-\sum_{i=1}^{M}f_{m,i}/M)^2}, \tag{2}$$

in which $f_{m,i}$ and $f_{p,i}$ are the measured and predicted probability values, respectively, for a given received intensity level corresponding to the $i$th bin, and $M$ is the total number of intensity bins. The probability density function (PDF) of each model and fitting results are presented next.

LD is mainly used in the literature to describe the fluctuations induced by weak atmospheric turbulence. In this case, the channel fading coefficient has the PDF of

$$f_h(h)=\frac{1}{2h\sqrt{2\pi\sigma^2}}\exp\left[-\frac{(\ln h-2\mu)^2}{8\sigma^2}\right], \tag{3}$$

where $\mu$ and $\sigma^2$ are the mean and variance of the distribution, respectively[12].

GD with shape parameter $k$ and scale parameter $\theta$ is expressed as

$$f_h(h)=\frac{1}{\Gamma(k)\theta^k}h^{k-1}\exp\left(-\frac{h}{\theta}\right), \tag{4}$$

where $\Gamma(k)$ is the gamma function[11].WD is used to excellently describe the atmospheric turbulence in a wide range of scintillation index values[15]. The Weibull PDF is defined as

$$f_h(h)=\frac{\beta}{\eta}\left(\frac{h}{\eta}\right)^{\beta-1}\exp\left[-\left(\frac{h}{\eta}\right)^{\beta}\right], \tag{5}$$

where the distribution parameters are $\beta$ and $\eta$.The PDF of GEVD is

$$f_h(h)=\frac{1}{\sigma}\left[1+k\left(\frac{h-\mu}{\sigma}\right)\right]^{\frac{-1}{k-1}}\exp\left\{\left[1+k\left(\frac{h-\mu}{\sigma}\right)\right]^{\frac{-1}{k}}\right\}, \tag{6}$$

and corresponding distribution parameters are $k$, $\mu$, and $\sigma$, where $k$ is a shape parameter.

By controlling the flow conversion ratio and changing the power of the air pump while keeping the aperture of the air pipe unchanged, the bubble size with different densities is generated. Hence, we can investigate the relationship between the statistical distribution of the received signal intensity under fluctuation and the bubble density.

Figure 4 compares the MD with different fitting models mentioned above under different bubble densities. It is observed that LD and GD perform close to the measurements and better than WD. The mean value of received signal intensity reduces with the increase of bubble density. When the bubble density is greater than a certain value, its influence on the received signal tends to be saturated. The fitting accuracy can be further observed from Table 2, where estimated distribution parameters of the statistical models under different bubble densities are also presented. In the table, L/G/W represents LD/GD/WD, respectively.

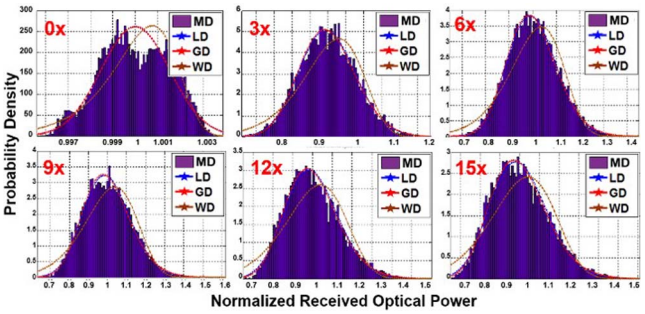


Fig. 4. Statistical distribution model fitting of received signal intensity under different bubble density.

**Table 2.** Fitting Accuracy and Distribution Parameters of the Statistical Models under Different Bubble Densities

| Bubble Density | | 0× | 3× | 6× | 9× | 12× | 15× |
|---|---|---|---|---|---|---|---|
| $\sigma^2_{I,m}$ | | 2.32 $e^{-6}$ | 6.2 $e^{-3}$ | 1.1 $e^{-2}$ | 1.55 $e^{-2}$ | 1.83 $e^{-2}$ | 2.13 $e^{-2}$ |
| L | GoF (%) | 89.3 | 98.2 | 99.0 | 98.3 | 98.1 | 96.8 |
| | $\mu$ | −6.6 $e^{-7}$ | −3.0 $e^{-3}$ | −5.5 $e^{-3}$ | −7.8 $e^{-3}$ | −8.9 $e^{-3}$ | −10 $e^{-3}$ |
| | $\sigma^2$ | 1.0 $e^{-3}$ | 7.9 $e^{-2}$ | 1.1 $e^{-1}$ | 1.2 $e^{-1}$ | 1.3 $e^{-1}$ | 1.4 $e^{-1}$ |
| G | GoF (%) | 89.3 | 98.2 | 98.9 | 98.0 | 97.3 | 95.7 |
| | $k$ | 7.6 $e^{+5}$ | 162 | 91 | 65 | 56 | 48 |
| | $\theta$ | 1.3 $e^{-6}$ | 6.2 $e^{-3}$ | 1.1 $e^{-2}$ | 1.5 $e^{-2}$ | 1.8 $e^{-2}$ | 2.1 $e^{-2}$ |
| W | GoF (%) | 89.1 | 89.2 | 89.7 | 89.4 | 84.7 | 82.9 |
| | $\beta$ | 1.00 | 1.04 | 1.05 | 1.06 | 1.06 | 1.06 |
| | $\eta$ | 1152 | 13.1 | 9.85 | 8.16 | 7.40 | 6.93 |

**Table 3.** Fitting Accuracy and Distribution Parameters of the Statistical Models under Different Bubble Sizes

| Bubble Size | | 0× | 3× | 6× | 9× | 12× | 15× |
|---|---|---|---|---|---|---|---|
| $\sigma^2_{I,m}$ | | 1.32 $e^{-6}$ | 9.76 $e^{-2}$ | 1.38 $e^{-1}$ | 1.46 $e^{-1}$ | 1.71 $e^{-1}$ | 1.84 $e^{-1}$ |
| L | GoF (%) | 89.3 | – | – | – | – | – |
| | $\mu$ | −6.6 $e^{-7}$ | – | – | – | – | – |
| | $\sigma^2$ | 1.0 $e^{-3}$ | – | – | – | – | – |
| G | GoF (%) | 89.3 | 5 | – | – | – | – |
| | $k$ | 7.6 $e^{+5}$ | 6.4 | – | – | – | – |
| | $\theta$ | 1.3 $e^{-6}$ | 1.6 $e^{-1}$ | – | – | – | – |
| W | GoF (%) | 89.1 | 28 | 2.7 | – | – | – |
| | $\beta$ | 1.00 | 1.10 | 1.11 | – | – | – |
| | $\eta$ | 1152 | 3.98 | 3.08 | – | – | – |
| GEVD | GoF (%) | – | 91.6 | 89.5 | 86.7 | 75.4 | 67.6 |
| | $k$ | – | −1.0 | −0.9 | −0.8 | −0.8 | −0.8 |
| | $\sigma^2$ | – | 3.32 $e^{-1}$ | 4.1 $e^{-1}$ | 4.2 $e^{-1}$ | 4.7 $e^{-1}$ | 4.9 $e^{-1}$ |
| | $\mu$ | – | 1.00 | 0.98 | 0.97 | 0.95 | 0.95 |

Similarly, we controlled the diameter of the air pipe and the power of the air pump to generate uniform bubbles of different sizes from 0× to 15× as in Table 1. Then, we considered model fitting under different bubble size settings. The results are presented in Fig. 5. As the bubble size increases, the channel fading deteriorates. The average intensity of received signals decreases, and the proportion of small signals becomes more evident. The signal distribution is, thus, very different from the case of changing the bubble density, since an increase of bubble size may severely block significant portions of the light beam. The fitting accuracy of GEVD is the highest, while the fitting results of the other three models are very poor.

To quantitatively evaluate the fitting performance, we further show the calculated GoF for different models in Table 3. We can see that GEVD performs the best, with the maximum GoF reaching 95%. When the bubble size to the beam diameter ratio is greater than 0.43 (3×), the LD cannot be fitted well; when the ratio is greater than 0.57 (6×), the GD does not work well; when the ratio is greater than 0.96 (9×), the WD fails. However, the GEVD can still yield an accuracy of 86.7% at this large bubble size, indicating that GEVD is relatively robust to bubble size variation.

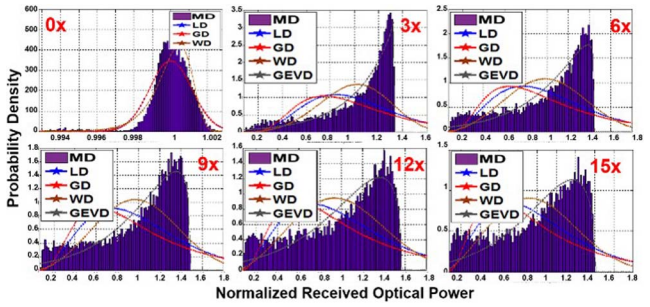


Fig. 5. Statistical distribution model fitting of received signal intensity under different bubble size.

With those understandings of bubble effects, the performance of a UOWC system in the bubble scenarios was further experimentally investigated. Different bubble density, bubble size, and data modulation are considered. The transmitter transmits 1 Gbps on–off keying (OOK) signals. The DC drive current and bias voltage for the laser source were set to 50 mA and 650 mV, respectively. At the receiver, APD210 was used to catch transmitted light, and the sampling rate of the OSC was 5 GSa/s.

The experimental bit error rate (BER) results for different bubble densities are shown in Fig. 6. We can observe that the BER performance of the system deteriorates seriously with the increase of bubble density. When the bubble density is greater than 12–15 cross-sections (3×) along the beam segment observed by the camera, the system BER is larger than the forward error correction (FEC) threshold of $3.8 \times 10^{-3}$ without post-equalization, and

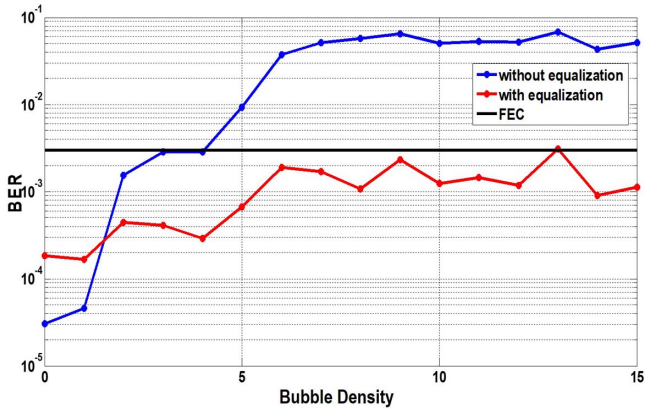


Fig. 6. BER performance versus bubble density.

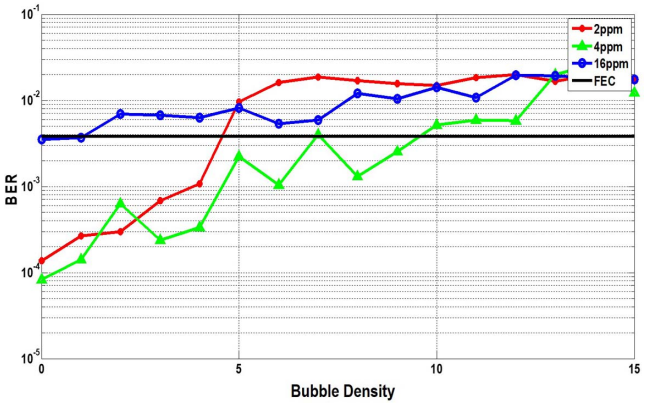


Fig. 8. BER performance versus bubble density under different PPM modulation orders.

the received signal cannot be demodulated correctly. As the bubble density increases to a level greater than 26 cross-sections (6×), the signal decay effect induced by the increased bubble density becomes more severe, and post-equalization techniques[16,17] are necessary to combat inter-symbol interference (ISI) induced by the light scattering of the bubbles. We adopted a nonlinear equalizer in a diagonal form of Volterra series, or equivalently a memory polynomial model as in Eq. (3) of the work[17], where the nonlinear order $K = 2$, and the maximum memory depth $Q = 8$. The equalizer performs well for a large range of bubble densities.

Similarly, we study the effects of bubble size and present the results in Fig. 7. When the bubble size to beam diameter ratio is greater than 0.57 (6×), the received signal cannot be demodulated correctly without post-equalization, but equalization helps to decrease the BER of the system from $7.29 \times 10^{-2}$ to $2.94 \times 10^{-3}$, which is below the FEC threshold.

Since the influence of the bubbles on the UOWC system is partially reflected in the signal attenuation caused by the occlusion of the optical path, it is worth investigating the influence of the effective signaling format and associated waveform temporal span on the communication system, such as pulse position modulation (PPM). So, we investigate the dependence of the system BER performance on bubble density and size under different PPM orders. At the transmitter, 2PPM, 4PPM, and 16PPM signals at 500 Mbps were transmitted. The DC drive current and bias voltage were set to 50 mA and 500 mV, respectively. At the receiver, APD210 was used to receive transmitted signals, and the sampling rate of the OSC was set to be 5 Gbps, 5 Gbps, and 10 Gbps corresponding to 2PPM, 4PPM, and 16PPM, respectively.

Figures 8 and 9 demonstrate the dependence of BER performance on bubble density and bubble size under different PPM modulation orders. With the increase of bubble density and size in a PPM modulation mode, the communication system performance degrades significantly. 2PPM and 4PPM perform satisfactorily for bubble density or bubble size up to 4×, but the increasing BER starts to cross the FEC threshold as density or size increases. The BER for 4PPM appears to increase more slowly as bubble density increases. 16PPM gives a BER higher than the FEC threshold for all testing values of bubble density and size. As compared to the OOK system, the PPM system is more sensitive to the bubble

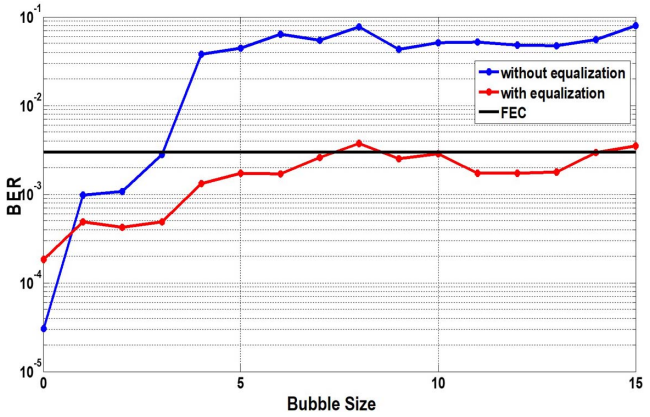


Fig. 7. BER performance versus bubble size.

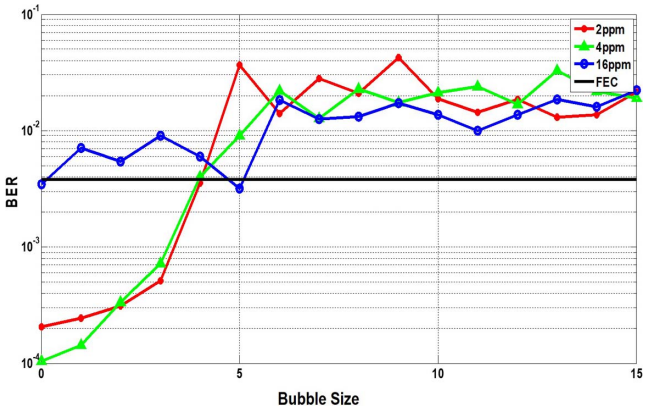


Fig. 9. BER performance versus bubble size under different PPM modulation orders.

conditions, and more sophisticated signal processing is necessary to reliably recover the PPM signals.

In summary, the performance of a UOWC system in a bubble scenario is related to the bubble density, bubble size, and modulation scheme. Probability distributions of received signal intensity significantly affect the system quality. The density and size change causes ISI change, whereas equalization can effectively improve the performance. Modulation schemes need to be properly chosen to match the channel characteristics. Further study on modulation and receiver design techniques under bubble induced channel attenuation and fading remains open for future work.

This work was supported by the National Key Basic Research Program of China (No. 2013CB329201), Key Program of National Natural Science Foundation of China (No. 61631018), Key Research Program of Frontier Sciences of CAS (No. QYZDY-SSW-JSC003), and Strategic Priority Research Program of CAS (No. XDA22000000).

## References

1. M.-A. Khalighi, C. Gabriel, T. Hamza, S. Bourennane, P. Léon, and V. Rigaud, in *Proceedings of 16th IEEE International Conference on Transparent Optical Networks* (2014), p. 1.
2. A. R. F. Barroso, G. Baiden, and J. Johnson, in *Proceedings of 7th IEEE International Conference on Ubiquitous and Future Networks* (2015), p. 727.
3. H.-J. Son, H.-S. Choi, N.-H. Tran, J.-H. Ha, D.-H. Ji, and J.-Y. Kim, Mod. Phys. Lett. B **29**, 1540023 (2015).
4. H. Uema, T. Matsumura, S. Saito, and Y. Murata, Electron. Commun. Japan **98**, 9 (2015).
5. P. L. Marston, S. C. Billette, and C. E. Dean, Proc. SPIE **925**, 308 (1988).
6. D. F. Gaitan and R. G. Holt, Phys. Rev. E **59**, 5495 (1999).
7. J. Cao, Y. Kang, and J. Wang, Laser Infrared **36**, 392 (2006).
8. L. Han and Y. L. Yuan, Sci. China Series D: Earth Sci. **50**, 1754 (2007).
9. R. M. Hagem, D. V. Thiel, S. G. O'Keefe, and T. Fickenscher, Microwave Opt. Technol. Lett. **54**, 729 (2012).
10. H. M. Oubei, R. T. ElAfandy, K.-H. Park, T. K. Ng, M.-S. Alouini, and B. S. Ooi, IEEE Photon. J. **9**, 7903009 (2017).
11. M. V. Jamali, A. Mirani, A. Parsay, B. Abolhassani, P. Nabavi, A. Chizari, P. Khorramshahi, S. Abdollahramezani, and J. A. Salehi, IEEE Trans. Commun. **66**, 4706 (2018).
12. M. V. Jamali, J. A. Salehi, and F. Akhoundi, IEEE Trans. Commun. **65**, 1176 (2017).
13. O. Korotkova, N. Farwell, and E. Shchepakina, Waves Random Complex Media **22**, 260 (2012).
14. L. C. Andrews and R. L. Phillips, *Laser Beam Propagation through Random Media* (SPIE, 2005).
15. R. A. Barrios and F. Dios, Opt. Eng. **52**, 046003 (2013).
16. B. Zhuang, C. Li, N. Wu, and Z. Xu, in *Proceedings of OSA Conference on Lasers and Electro-Optics (CLEO)* (2017), paper STh3O.3.
17. X. Li, H. Chen, S. Li, Q. Gao, C. Gong, and Z. Xu, in *Proceedings of 13th IEEE International Wireless Communications and Mobile Computing Conference (IWCMC)* (2017), p. 616.